

# Improved resolution and sensitivity on the ANSTO microprobe and its application to $\mu$ -PIXE

R. Siegele<sup>a,\*</sup>, A.G. Kachenko<sup>b</sup>, M. Ionescu<sup>a</sup>, D.D. Cohen<sup>a</sup>

<sup>a</sup> Institute for Environmental Research, Australian Nuclear Science and Technology Organisation (ANSTO), PMB1, Menai, NSW 2234, Australia

<sup>b</sup> Faculty of Agriculture, Food and Natural Resources, The University of Sydney, NSW 2006, Australia

## ARTICLE INFO

Available online 12 March 2009

### PACS:

07.85.Nc  
29.27.-a  
41.75.Ak  
41.85.Lc  
89.60.-k

### Keywords:

Elemental localisation  
*Hybanthus floribundus*  
Metal hyperaccumulation  
Micro-PIXE  
Nickel (Ni)  
Nuclear microprobe

## ABSTRACT

We report on the improved spatial resolution of the ANSTO heavy ion microprobe, achieved through the use of a higher brightness ion source for hydrogen. The improved resolution will be demonstrated for applications of  $\mu$ -PIXE.

With the higher brightness source, a 3  $\mu$ m resolution was achieved for  $\mu$ -PIXE elemental analysis. This is illustrated in high resolution images of nickel (Ni)-hyperaccumulating *Hybanthus floribundus* subsp. *floribundus* leaf tissues, where individual cells were clearly visible in the acquired elemental images. The higher resolution images illustrated that Ni was localised in epidermal cell walls.

Crown Copyright © 2009 Published by Elsevier B.V. All rights reserved.

## 1. Introduction

Microprobe analysis strives to continuously improve both spatial resolution and sensitivity. Over the last couple of years, the Australian Nuclear Science Technology Organisation (ANSTO) heavy ion nuclear microprobe (HINMP) [1] and the Australian National Tandem Research (ANTARES) accelerator facility [2] have undergone a number of improvements to increase target currents in order to enhance resolution and sensitivity.

The spatial resolution of a microbeam is determined by several parameters, such as focussing power and aberrations of the beam forming lens system, stray magnetic and electric fields and mechanical vibrations [3]. Another important factor is the brightness of the ion source. Although the brightness does not directly influence the spot size, it determines the beam current available for analysis at a given spot size [3]. The 10 MV ANTARES accelerator has two sputter ion sources in addition to a He ion source (Alphatross) from NEC. One of the sputter ion sources is a Model 860 negative ion source originally from the General Ionex Corporation, which has an annular ioniser. The second ion source is a Model 846 multi-sample ion source from High Voltage Engineering developed for Accelerator Mass Spectrometry (AMS) measure-

ments. This ion source has a spherical ioniser and can produce a high current output of up to 100  $\mu$ A.

Our original assessment of both ion sources showed that the multi-sample ion source had a higher current output, however, on target the same beam current could be achieved using the Model 860 ion source. This was due to vertical misalignment between the ion source and the microprobe [4]. Recently, this multi-sample ion source (Model 846) has been refurbished and optimised [2], which prompted us to re-evaluate the use of this ion source for microprobe experiments. We show a comparison of the two sputter ion sources.

In this paper, we report on our progress towards improving the target current for a given spot size by optimising the ion source and the beam transmission to the microprobe. We also present an example of improved resolution and sensitivity of the microprobe using leaf tissues from Ni hyperaccumulating *Hybanthus floribundus* subsp. *floribundus* (Violaceae).

## 2. Methods and materials

### 2.1. Experimental

To improve the performance of the microprobe, we have undertaken major upgrades in various areas, such as electronics, data

\* Corresponding author. Tel.: +61 2 9717 3967; fax: +61 2 9717 3257.  
E-mail address: [rns@ansto.gov.au](mailto:rns@ansto.gov.au) (R. Siegele).

acquisition but most importantly the ion source. Over the past few years, the brightness of the Model 860 ion source has been steadily diminishing, with the output of the ion source decreasing from around  $4 \mu\text{A}$  to less than  $1 \mu\text{A}$ . Conversely, the second sputter ion source on the ANTARES accelerator, a Model 846 multi-sample AMS source can produce proton beam currents greater than  $10 \mu\text{A}$ . However, vertical misalignment of this ion source relative to the microprobe did not allow us to take full advantage of its brightness and as a consequence, the difference in beam current on the target from both ion sources was quite small.

Recently, the multi-sample AMS ion sources was completely rebuilt and realigned and the transmission to the microprobe re-evaluated. Additionally, a horizontal steerer was added behind the object slits of the microprobe to steer the beam vertically and correct for any misalignment of the ion source. This improved the target current by a factor of 10.

Historically, we have achieved a beam current of typically 2–5 nA into a spot size of  $10 \mu\text{m}$  for 3 MeV protons. This spot size is achieved with an acceptance of  $0.03 \text{ mm}^2 \text{ mrad}^2$ , which indicates a normalised brightness between 4.5 and  $12.2 \times 10^{-3} \text{ Am}^{-2} \text{ rad}^{-2} \text{ eV}^{-1}$ . However, this is not the brightness of the ion source but the beam brightness at the microprobe entrance after its transmission through the tandem accelerator. We have increased this target current to 10–20 nA for 3 MeV protons

and  $10 \mu\text{m}$  spot size, which achieved a spot size of 1–2  $\mu\text{m}$  with approximately 100 pA. The spot size was verified by scanning the beam across a silicon wafer with  $50 \times 50 \mu\text{m}$  squares of Cr and Au deposited on it. Fig. 1 shows the Cr and Au profiles across the edge together with the fit using an error function. The fits showed a beam spot size between 1 and 2  $\mu\text{m}$ . This indicates a considerable improvement over our previous spot size of 3  $\mu\text{m}$ . More importantly, we are now able to achieve about 0.5 nA into a spot size of 3  $\mu\text{m}$ . This is a considerable improvement over previously achieved currents of about 0.1 nA, and reduces our analysis time by a factor of 5.

To ascertain if this was the smallest spot size that could be achieved with our current setup, we used scanning transmission ion microscopy (STIM) on copper mesh and a current of a few hundred particles per second. With these very small currents we measured a spot size of 0.5–1.0  $\mu\text{m}$  (see Fig. 2). This is likely to be the limit that can be currently achieved on the ANSTO microprobe, unless additional steps are performed to reduce magnetic stray fields and vibrations in the system.

## 2.2. Sample preparation

In this study, elemental distribution in leaf tissues of the Ni hyperaccumulating *H. floribundus* subsp. *floribundus* was investigated using the HINMP. This perennial shrub species can naturally accumulate up to  $13,500 \text{ mg Ni kg}^{-1}$  in leaf tissues on a dry weigh (DW) basis [5]. Plants were grown under controlled glasshouse conditions and exposed to  $1500 \text{ mg Ni kg}^{-1}$  (applied as a  $\text{Ni-SO}_4 \cdot 6\text{H}_2\text{O}$  solution). Following 20 weeks of growth, plants were harvested and leaf tissues prepared using freeze-drying and freeze-substitution protocols reported elsewhere [6,7]. Owing to the thickness of freeze-dried samples ( $50 \mu\text{m}$ ), high resolution elemental mapping was not achievable. In order to make use of higher resolution spot sizes, thinner sections ( $10 \mu\text{m}$ ) prepared by freeze-substitution were utilised [7,8].

## 2.3. Microprobe analysis

Samples were analysed using a 3 MeV H beam with a spot size of 3  $\mu\text{m}$  and beam current of 0.5–1 nA. X-rays were detected using a  $100 \text{ mm}^2$  Ge detector with a solid angle of 90 msr. The detector had a  $25 \mu\text{m}$  Be window and a  $100 \mu\text{m}$  thick Mylar foil was placed in front of the detector to prevent scattered protons from entering the detector and reduce the low energy X-ray yield from light elements. Data were acquired using the Data Acquisition System

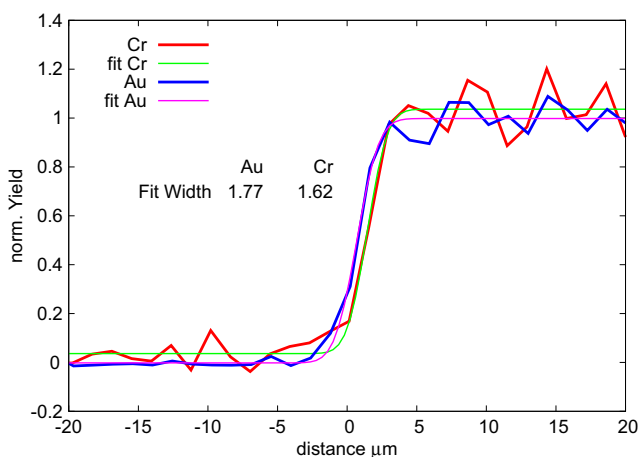


Fig. 1. X-ray yield as the beam is scanned across the edge of the Cr/Au layer, showing an effective spot size between 1 and 2  $\mu\text{m}$ .

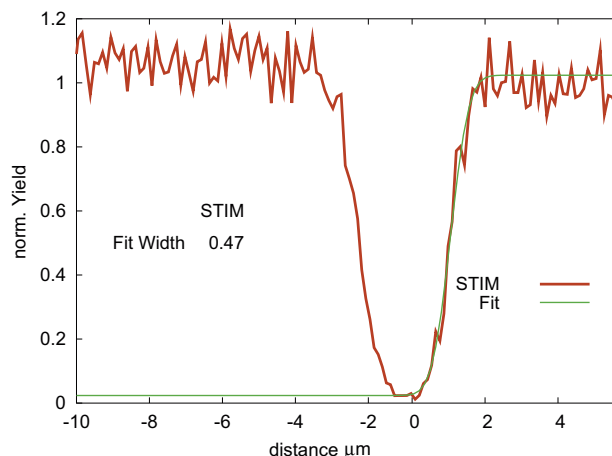
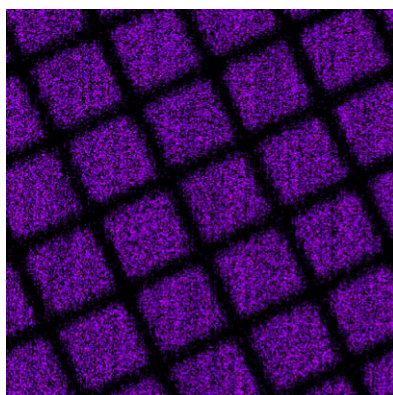


Fig. 2. A scanning transmission ion microscopy (STIM) map across a 2000 lines per inch copper grid. The graph on the right shows a transmission scan across one of the wires. The resulting fits are also presented.

mpsys4 from Melbourne University together with a Canberra Model 2060 digital signal processor. GeoPIXE 2 software was used to extract the elemental concentration maps [9,10].

### 3. Results and discussion

Fig. 3 presents a Ca and Ni map of a freeze-substituted *H. floribundus* subsp. *floribundus* leaf section. The elemental maps were generated from a 2 hours scan, with a target current of 0.8 nA accumulating a total charge of 5.7  $\mu\text{C}$ . This resulted in images with very good resolution that clearly showed that both Ca and Ni were localised in the cell walls of the epidermis, while Ni and Ca concen-

tration within the epidermal cells was minimal. This observation is supported by elemental profiles shown in Fig. 4, which were taken along the dotted white line indicated in Fig. 3. The lines that define the epidermis layer are drawn through the cell walls and show a clear maximum for Ca on both the inner and outside cell wall, while for Ni, a clear maximum on the outside cell walls was observed. However, this finding may be related to elemental redistribution as previously reported [7].

Previous Ca and Ni maps taken on an adjacent sample from the same freeze-substituted *H. floribundus* subsp. *floribundus* leaf section were acquired at a much lower beam current of 0.1 nA [7]. Although these maps were taken with a similar spot size of 3  $\mu\text{m}$ , they were not as clear as the maps shown here, because of the lower available beam current. Despite the apparent redistribu-

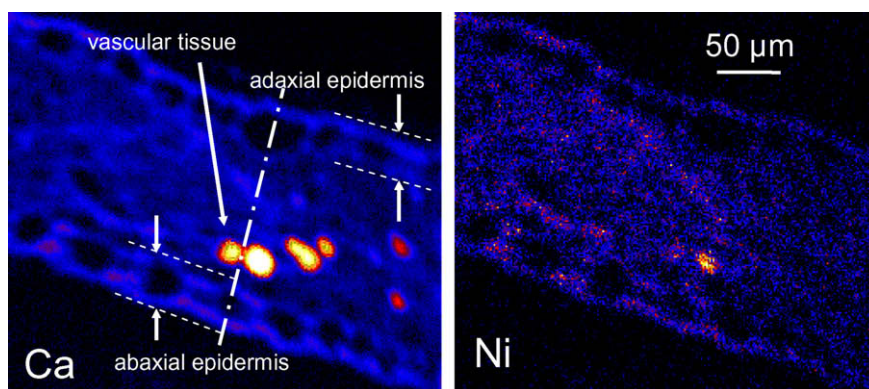


Fig. 3. Quantitative elemental maps showing distribution of Ca and Ni in a freeze-substituted *Hybanthus floribundus* subsp. *floribundus* leaf section. The dotted line corresponds to the profile plotted in Fig. 4.

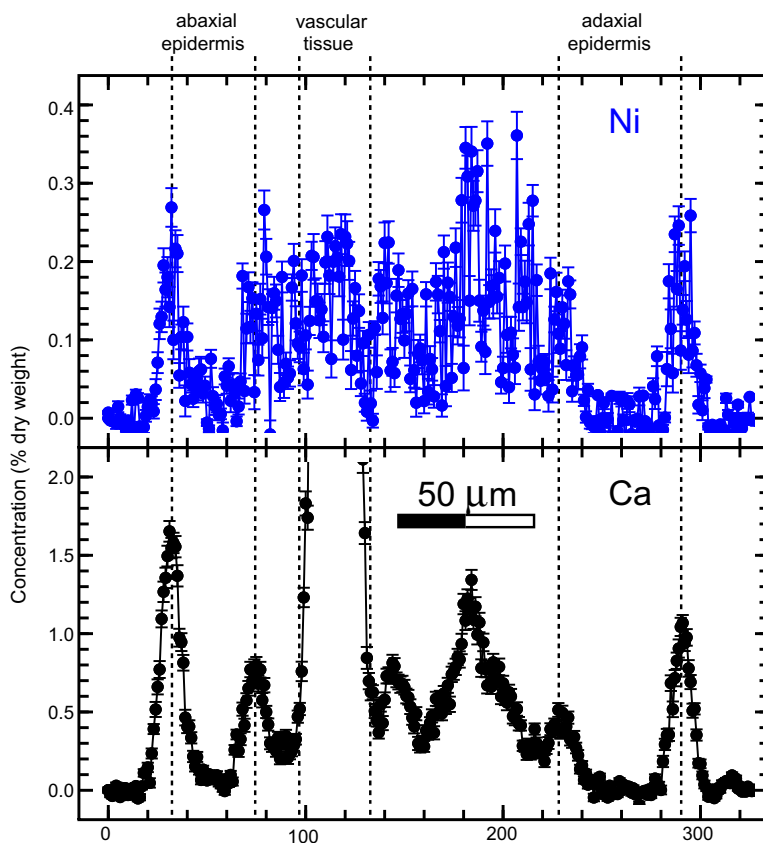
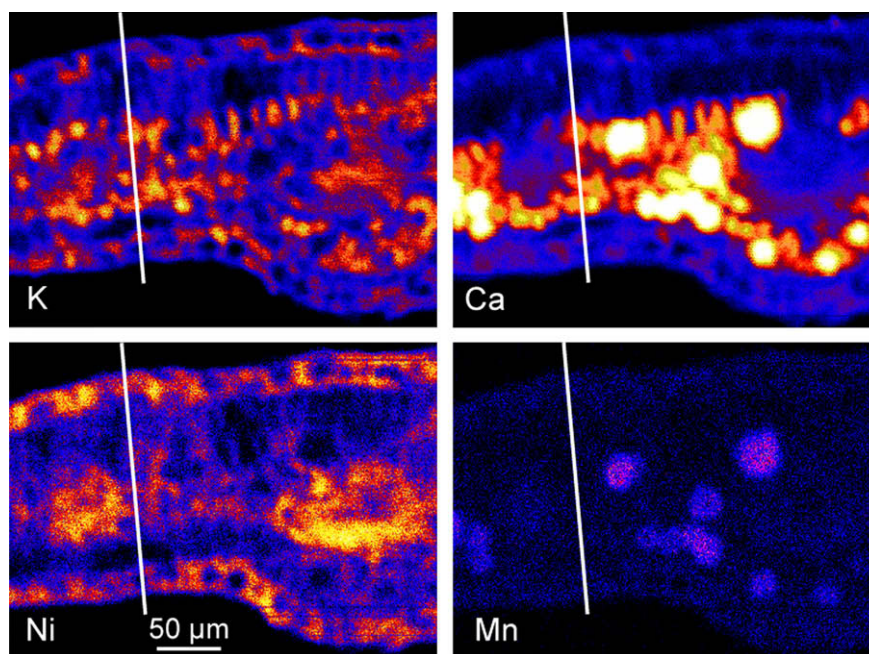


Fig. 4. Quantitative elemental profiles of Ni and Ca across a freeze-substituted *Hybanthus floribundus* subsp. *floribundus* leaf section.



**Fig. 5.** High resolution elemental maps showing distribution of K, Ca, Ni and Mn in a freeze-dried leaf cross-section of *Hybanthus floribundus* subsp. *floribundus*. The line corresponds to the profile plotted in Fig. 7.

tion of Ni and Ca during the freeze-substitution procedure, these samples are well suited to demonstrate the improved resolution of the microprobe.

To further investigate if Ca and Ni are concentrated inside the epidermis walls or to ascertain if this is an artefact caused by the freeze-substitution of samples, elemental maps were obtained using a freeze-dried *H. floribundus* subsp. *floribundus* leaf section (Fig. 5). Our previous results have indicated that  $\mu$ -PIXE measurements of elements in freeze-dried *H. floribundus* subsp. *floribundus* tissues are comparable to ICP results [11,12]. Owing to the thickness of freeze-dried samples (30–50  $\mu$ m), these maps illustrate the average elemental concentration of the tissue imaged. Therefore, individual cells are less apparent than in freeze-substituted maps (Fig. 3), however the leaf anatomy can still be distinguished quite well in the maps.

In the present study, the Ni distribution in freeze-dried *H. floribundus* subsp. *floribundus* leaf tissue was not uniform and concurred with our previous studies that indicated adaxial epidermal cells as the preferential site of Ni localisation [7,12]. Lowest Ni distribution occurred in the spongy mesophyll tissue which is also in agreement with our earlier studies. In Fig. 6, a light micrograph of a stained leaf section is presented to depict the anatomical structure of the leaf. Comparing the light micrograph with the elemental maps, the adaxial and abaxial epidermis is clearly distinguished by their higher K and Ni concentrations compared to the adjacent tissues.

Below the adaxial epidermis and above the abaxial epidermis, a cell layer is visible, distinguished by a lower concentration in Ni, K and Ca compared to the epidermis and concurs with the position of the palisade mesophyll. The palisade layer below the adaxial epidermis shows elongated cells, which are typical for the palisade mesophyll layer (Fig. 6). Below the upper palisade layer, a second layer of elongated cells is clearly visible which has a much higher K and Ca content. These palisade layers are faintly indicated in the acquired  $\mu$ -PIXE images (Fig. 5). The Ni concentration in both layers was similar, but lower than in epidermal tissues. A high concentration of Ni was also observed in the vascular tissue, most likely in the xylem tissues.

Fig. 7 shows concentration profiles taken across the leaf section in Fig. 5. The profiles show two maxima in the Ni, K and Ca concentration in the abaxial epidermis, which are close to the cell walls of this layer. This indicates a higher concentration of all three elements in the walls of the epidermis cells compared to the cell contents. However, the maxima are less pronounced compared to concentration profiles of the freeze-substituted sample and only broad maxima are visible in the adaxial epidermis. This is because the sample is much thicker and concentration profiles depict the average over a number of cell layers stacked on top of each other. Nevertheless, these results indicate that Ca, Ni and K are indeed concentrated in the cell walls, which has also been observed in *H. floribundus* subsp. *adpressus* using energy dispersive X-ray microanalysis [13]. The high current also enabled us to map elements such Mn which is only present at a concentration of 100–200  $\text{mg kg}^{-1}$  with sufficient statistics. The Mn map showed that its distribution was similar to Ca.

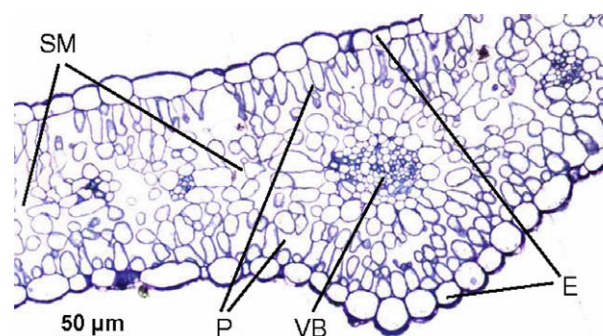


**Fig. 6.** Light micrograph of a Ni-treated leaf cross-section of *Hybanthus floribundus* subsp. *floribundus* (1  $\mu$ m, magnification  $\times 40$ ); where E, epidermis; P, palisade mesophyll; SM, spongy mesophyll and VB, vascular bundle.

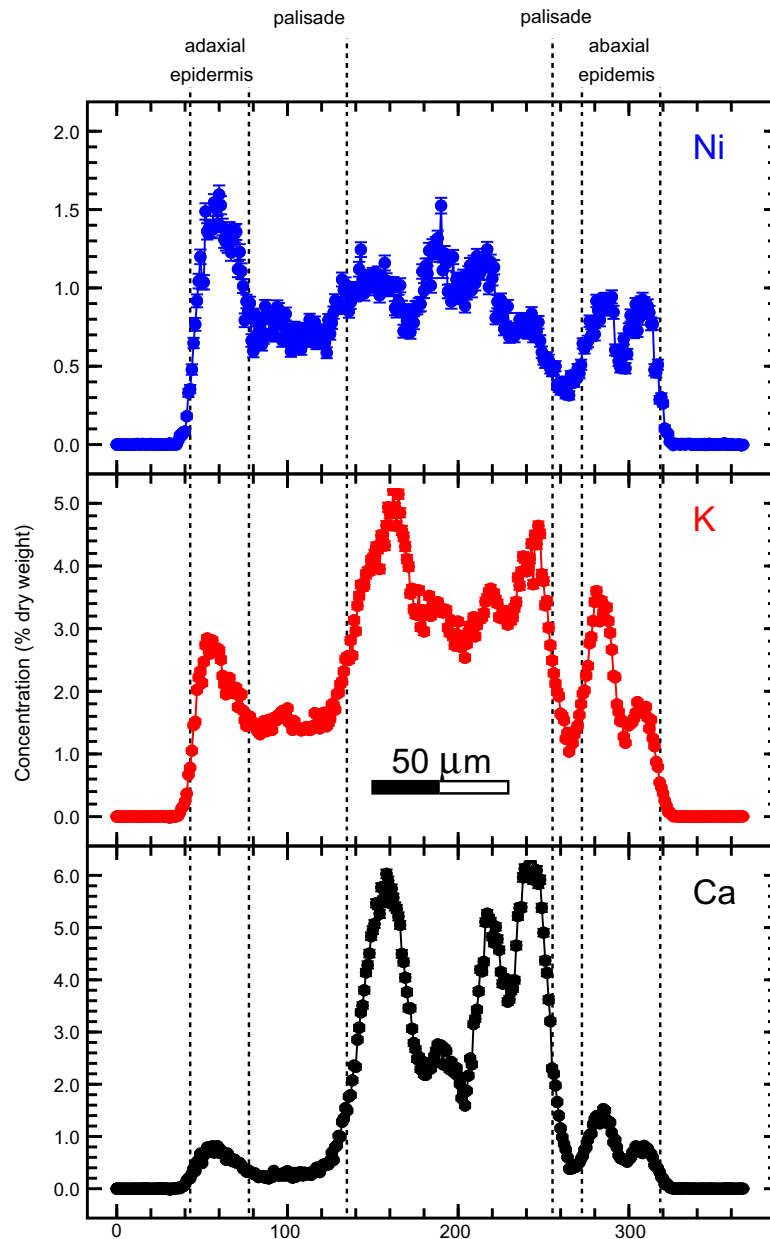


Fig. 7. Quantitative elemental profiles of Ni, K and Ca across a freeze-dried *Hybanthus floribundus* subsp. *floribundus* leaf section.

#### 4. Conclusions

By optimising the ion source and applying additional steering we have been able to increase the ion source current to almost 1 nA into a 3  $\mu\text{m}$  spot size. This enabled us to achieve higher resolution images with individual cell layers visible in the elemental maps taken from leaf sections of the Ni hyperaccumulating plant *H. floribundus* subsp. *floribundus*. Thin samples prepared by freeze-substitution showed sub-cellular resolution in the elemental maps with the cell walls of the epidermis cells clearly showing a higher Ca and Ni concentration compared with the cell plasma. Freeze-dried samples also showed a higher Ca and Ni concentration in the cell walls, which confirms that both elements are concentrated in the cell walls.

#### Acknowledgements

The authors thank Kevin Ansary for his help in running the Tandem Accelerator and the Tandem Accelerator Operations Team for

their efforts. A.G. Kachenko acknowledges funding received from the Australian Institute of Nuclear Science and Engineering (AINSE) and the Australian Government through an Australian Postgraduate Award scholarship.

#### References

- [1] R. Siegele, D.D. Cohen, N. Dytlewski, Nucl. Instr. and Meth. B 158 (1999) 31.
- [2] David Garton, Kevin Ansary, Peter Drewer, in: SNEAP 2005 Proceedings, submitted for publication; David Garton, Greg Cooke, in: SNEAP 2007 Proceedings, submitted for publication.
- [3] G.J. F Legge, P.M. O'Brian, R.M. Sealock, G.L. Allan, G. Bench, G. Moloney, D.N. Jamieson, A.P. Mazzolini, Nucl. Instr. and Meth. B 30 (1988) 252.
- [4] D.D. Cohen, R. Siegele, N. Dytlewski, ANSTO E-Report 727, 1996.
- [5] M.E. Farago, I.E.D.A.W. Mahmoud, Environ. Geochem. Health 5 (1983) 113.
- [6] N.P. Bhatia, K.B. Walsh, I. Orlic, R. Siegele, N. Ashwath, A.J.M. Baker, Fun. Plant Biol. 31 (2004) 1061.
- [7] A.G. Kachenko, R. Siegele, N.P. Bhatia, B. Singh, M. Ionescu, Nucl. Instr. and Meth. B 266 (2008) 1598.
- [8] E. Pålsgård, U. Lindh, G.M. Roomans, Microsc. Res. Technol. 28 (1994) 254.
- [9] C.G. Ryan, Int. J. Imag. Syst. Technol. 11 (2000) 219.

- [10] C.G. Ryan, Nucl. Instr. and Meth. B 181 (2001) 170.
- [11] R. Siegele, A.G. Kachenko, N.P. Bhatia, Y.D. Wang, M. Ionescu, B. Singh, A.J.M. Baker, D.D. Cohen, X-Ray Spectrom. 37 (2008) 133.
- [12] A.G. Kachenko, B. Singh, N.P. Bhatia, R. Siegele, Nucl. Instr. and Meth. B 266 (2008) 667.
- [13] S.D. Bidwell, S. Crawford, I. Woodrow, J. Sommer-Knudsen, A. Marshall, Plant Cell Environ. 27 (2004) 705.